

Tailoring High-Frequency Magnonics in Monolayer Chromium Trihalides

Raí M. Menezes,^{1,2,3} Denis Šabani,^{1,2} Cihan Bacaksiz,^{1,2} Clécio C. de Souza Silva,³ and Milorad V. Milošević^{1,2,*}

¹*Department of Physics, University of Antwerp, Groenenborgerlaan 171, B-2020 Antwerp, Belgium*

²*NANOLab Center of Excellence, University of Antwerp, Belgium*

³*Departamento de Física, Universidade Federal de Pernambuco, Cidade Universitária, 50670-901, Recife-PE, Brazil*

(Dated: November 30, 2021)

Monolayer chromium-trihalides, the archetypal two-dimensional (2D) magnetic materials, are readily suggested as a promising platform for high-frequency magnonics. Here we detail the spin-wave properties of monolayer CrBr₃ and CrI₃, using spin-dynamics simulations parametrized from the first principles. We reveal that spin-wave dispersion can be tuned in a broad range of frequencies by strain, paving the way towards flexo-magnonic applications. We further show that ever-present halide vacancies in these monolayers host sufficiently strong Dzyaloshinskii-Moriya interaction to scatter spin-waves, which promotes design of spin-wave guides by defect engineering. Finally we discuss the spectra of spin-waves propagating across a moiré-periodic modulation of magnetic parameters in a van der Waals heterobilayer, and show that the nanoscale moiré periodicities in such samples are ideal for realization of a magnonic crystal in the terahertz frequency range. Recalling the additional tunability of magnetic 2D materials by electronic gating, our results situate these systems among the front-runners for prospective high-frequency magnonic applications.

1. Introduction

Two-dimensional (2D) magnetic materials, such as monolayer chromium trihalides and manganese dichalcogenides, have recently drawn immense attention of both theoretical and experimental research, due to their fundamental significance and promising technological applications. The high tunability of the magnetic interactions in such materials, e.g., by lattice straining^{1,2}, electronic gating^{3,4}, and layer stacking⁵⁻⁷, among other techniques, directly leads to manipulation of magnetic textures, such as domain-walls, spin-waves (SWs) and magnetic skyrmions, thus opening a range of possibilities for novel device concepts⁸. Arguably, the largest impact of these manipulations can be realized in the field of magnonics, considering that magnons have been readily detected in atomically-thin chromium tri-iodide⁹, with documented spin-wave modes even in terahertz frequencies¹⁰. Further advances on that front would make 2D magnetic materials the prime candidates for ultra-fast information transport and processing based on magnonics.

In a chromium trihalide monolayer CrX₃ (with X = I, Br or Cl), Cr atoms form a planar honeycomb structure sandwiched between two atomic planes of the halogen atoms, as illustrated in Fig. 1. The ferromagnetic superexchange across the Cr-X-Cr bonds is anisotropic, which together with the weak single-ion anisotropy of Cr results in a ferromagnetic order with off-plane easy axis^{11,12}. In addition to the symmetric exchange, the antisymmetric exchange, also known as the Dzyaloshinskii-Moriya interaction (DMI), can be awoken in such systems with any structural or electronic asymmetry seen by Cr atoms, such as present in e.g. Janus monolayers¹³ or in applied electric field^{14,15}.

In this work we investigate the SW propagation in monolayer CrBr₃ and CrI₃ as exemplary representa-

tives of 2D magnetic materials. We obtain all relevant magnetic parameters from first-principle calculations on the considered structures^{1,16}, and perform spin-dynamics simulations of the SW propagation. We proceed to calculate the SW dispersion relation in the chromium trihalides under strain, revealing the tunability of magnonic behavior by strain-engineering. We further analyse the role of ever-present lattice defects (halide vacancies) in considered monolayers, usually assumed detrimental for the spin-wave propagation. We show that such lattice defects induce local DMI, which can indeed strongly affect the SW dynamics, but can be proven useful rather than detrimental – for example, a tailored pattern of defects can confine the SWs and serve as a SW guide. Finally, we report the spectra of SWs propagating across periodic modulation of the magnetic parameters, induced by the moiré pattern of a van der Waals heterobilayer^{17,18}. We show that such samples, readily made experimentally, can function as a magnonic crystal¹⁹ for the high-frequency SWs, exhibiting band gaps of propagating SW frequencies. Coupled to the wide range of manipulations available in 2D materials, our results clearly indicate a number of promising directions for terahertz magnonics in magnetic monolayers.

2. Atomistic spin simulations

In the simulations we consider a spin system arranged in a honeycomb structure in order to mimic the magnetic moments of Cr atoms in the chromium trihalide monolayer. To reduce the magnetic behavior of the entire monolayer to just the simulation within the Cr plane is made possible by *ab initio* parametrization of microscopic magnetic interactions for different considered cases, done according to Refs. 1 and 16, where we performed *ab initio* four-state energy mapping (4SM) based on density functional theory (DFT) calculations. For more details on the method

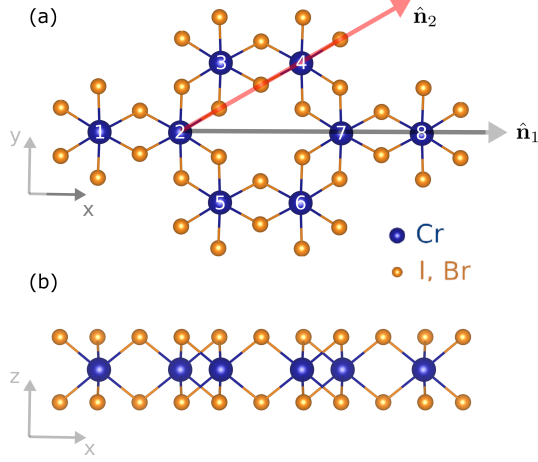


FIG. 1. (a) Top view of the CrX_3 lattice. $\hat{\mathbf{n}}_1$ and $\hat{\mathbf{n}}_2$ represent the main symmetry axes discussed in Sec. 3. (b) Side view of the CrX_3 monolayer.

we refer to Ref. 20.

In the spin simulations we consider the quadratic Heisenberg spin Hamiltonian, given by

$$\mathcal{H} = \frac{1}{2} \sum_{i,j} \mathbf{S}_i \mathcal{J}_{ij} \mathbf{S}_j + \sum_i \mathbf{S}_i \mathcal{A}_i \mathbf{S}_i. \quad (1)$$

Here \mathcal{J}_{ij} and \mathcal{A}_i are the exchange and single ion anisotropy (SIA) matrices, respectively, and $\mathbf{S}_i = (S_i^x, S_i^y, S_i^z)$ is the spin vector at the i^{th} site. We consider $S = 3/2$ for the Cr^{3+} ions, with 3 unpaired valence electrons and quenched orbital moment ($L = 0$), which yields a magnetic moment of $\sim 3\mu_B$ per Cr atom, in agreement with the experimental observations^{11,12,20–22}.

The sum over i in Eq. (1) runs over all Cr sites, while the sums over i, j run over all nearest-neighbor Cr pairs. The exchange matrix can be further decomposed into a symmetric exchange J and the antisymmetric DMI vector \mathbf{D} . The Hamiltonian then becomes

$$\begin{aligned} \mathcal{H} = & \frac{1}{2} \sum_{i,j} \left[J_\alpha S_i^\alpha S_j^\alpha + J_\beta S_i^\beta S_j^\beta + J_\gamma S_i^\gamma S_j^\gamma \right. \\ & \left. + \mathbf{D}_{ij} \cdot (\mathbf{S}_i \times \mathbf{S}_j) \right] \\ & + \sum_i \left[\mathcal{A}_{\alpha'} (S_i^{\alpha'})^2 + \mathcal{A}_{\beta'} (S_i^{\beta'})^2 + \mathcal{A}_{\gamma'} (S_i^{\gamma'})^2 \right], \end{aligned} \quad (2)$$

where $\{\alpha\beta\gamma\}$ and $\{\alpha'\beta'\gamma'\}$ are the local bases of eigenvectors that diagonalize J and \mathcal{A} , respectively. $S_i^u = \frac{\mathbf{u} \cdot \mathbf{S}_i}{|\mathbf{u}|}$ is the projection of the i^{th} spin along the vector \mathbf{u} . For simplicity, and since in this work we are interested in high frequency SWs dominated by the short-range exchange interactions, we neglect the contributions of dipole-dipole interactions. Notice that the above Hamiltonian is not limited to isotropic exchange interactions, and can be applied to different atomistic structures, e.g. including lattice defects where the bases of eigenvectors can change

pair ($i-j$)	J^{xx} (meV)	J^{yy} (meV)	J^{zz} (meV)	J^{xy} (meV)	J^{xz} (meV)	J^{yz} (meV)
CrI₃						
(1-2)	-5.10	-3.72	-4.63	0.00	0.00	0.84
(2-3)	-4.07	-4.76	-4.63	-0.60	0.72	-0.42
(2-5)	-4.07	-4.76	-4.63	0.60	-0.72	-0.42
$\langle J \rangle$	-4.41	-4.41	-4.63	0.00	0.00	0.00
CrBr₃						
(1-2)	-3.45	-3.29	-3.42	0.00	0.00	0.10
(2-3)	-3.33	-3.41	-3.42	-0.07	0.08	-0.05
(2-5)	-3.33	-3.41	-3.42	0.07	-0.08	-0.05
$\langle J \rangle$	-3.37	-3.37	-3.42	0.00	0.00	0.00
Δ	\mathcal{A}^{zz}					
	(meV)	(meV)				
CrI ₃	-0.22	-0.07				
CrBr ₃	-0.04	-0.01				

TABLE I. Magnetic parameters for pristine CrI_3 and CrBr_3 obtained from first-principle calculations [see Ref. 1 for details]. J^{xx} , J^{yy} , and J^{zz} are diagonal elements, and $J^{xy} = J^{yx}$, $J^{xz} = J^{zx}$, $J^{yz} = J^{zy}$ the off-diagonal elements of the exchange matrix. $\langle J \rangle$ is the average exchange over the three nearest-neighbour pairs and $\Delta = \langle J^{xx} \rangle - \langle J^{zz} \rangle$ is the out-of-plane anisotropy. \mathcal{A}^{zz} is SIA parameter, same for each Cr site. Pairs ($i-j$) are indicated in Fig. 1 (a).

for specific bonds. For either considered structure, corresponding exchange matrices for different Cr pairs are obtained from first principles calculations. Table I lists the magnetic parameters obtained for pristine CrI_3 and CrBr_3 monolayers. Parameters obtained for other specific cases considered in this paper will be shown where needed.

To simulate the magnonic behavior, we resort to spin dynamics captured by the Landau-Lifshitz-Gilbert (LLG) equation

$$\frac{\partial \hat{\mathbf{S}}_i}{\partial t} = -\frac{\gamma}{(1 + \alpha^2)\mu} \left[\hat{\mathbf{S}}_i \times \mathbf{B}_i^{\text{eff}} + \alpha \hat{\mathbf{S}}_i \times (\hat{\mathbf{S}}_i \times \mathbf{B}_i^{\text{eff}}) \right], \quad (3)$$

where γ is the electron gyromagnetic ratio, α is the damping parameter, μ is the magnetic moment per Cr atom, and $\mathbf{B}_i^{\text{eff}} = -\partial \mathcal{H} / \partial \hat{\mathbf{S}}_i$ is the effective field. In this work, the LLG spin dynamics simulations are primarily based on the simulation package *Spirit*²³, adapted to accommodate our (Kitaev) Hamiltonian [Eq. (2)].

3. Strain-tunable spin-wave propagation in CrX_3 monolayers

The magnetic interactions in 2D materials are very sensitive to any deformation in the atomic lattice. In particular, it has been shown that exchange interactions in CrI_3 and CrBr_3 are significantly affected by either tensile or compressive strain¹. Therefore, in this section, we discuss how straining the material can affect the propagation of SWs in magnetic monolayers. For the simulations, we consider both CrBr_3 and CrI_3 monolayers in their pristine form, as well as under uniform biaxial

strain. The SW beams are artificially created by a sinusoidal in-plane oscillating field $\mathbf{B}_{\text{input}} = b_0 \sin(2\pi f_{\text{in}} t) \hat{k}$ applied in a narrow rectangular region^{24,25}, where f_{in} is the input frequency, b_0 the field amplitude, and \hat{k} the SW propagation direction. In the simulations we consider $b_0 = 0.1$ T and damping parameter $\alpha = 0.001$. The SW frequency f and wavelength λ are calculated by fitting a sine function to the magnetization oscillations [see e.g. Fig.2 (a)] as a function of time and space respectively. Fig. 2 (b,c) shows the dispersion relation, i.e., the relation between the SW frequency and the wavenumber $k = 2\pi/\lambda$ for CrBr₃ and CrI₃, respectively, obtained for materials under different strain. The calculated dispersion curves correspond to the lower-energy magnon modes. Notice that the SW dispersion can be tuned throughout a wide range of frequencies by straining the honeycomb structure, which actually demonstrates the ease of tuning magnonics in such 2D materials. Solid lines in Fig. 2 (b,c) depict the fit of the quadratic expression $f(k) = Ak^2 + f_0$ to the numerical data. The values of the fitting parameters A and f_0 as a function of strain are shown in Fig. 2 (d). One can clearly notice the distinctly different response of the parameter f_0 , which corresponds to the zero-momentum SW mode, to strain in CrBr₃ and CrI₃. As discussed below, this behaviour is directly related to the out-of-plane exchange anisotropy, whose magnitude for CrI₃ increases for either tensile or compressive strain, while for CrBr₃ it changes linearly with strain [see, e.g., Fig S1 in the supplemental material²⁶]. The corresponding energy gap at $k = 0$, given by $\Delta E = hf_0$, where h is the Plank constant, varies in the range of 1.25 to 1.74 meV for CrI₃ and from 0.18 to 0.36 meV for CrBr₃, under the -5 to 5 % range of strain. Those values have the same order of magnitude, but are significantly smaller than those measured for the case of few layer CrI₃ in Ref. 10 (9.4 meV) and Ref. 27 (3 meV). Despite this quantitative discrepancy, we expect that the here reported strain engineering of spin-wave excitations, manifesting differently in different Cr-trihalide monolayers, can be validated by experimental techniques^{10,27-30}.

The SW dispersion can be obtained analytically in the limit of small SW amplitude by solving the linearized LLG equation³¹. For that purpose, let us simplify the Hamiltonian [Eq. (2)] as follows. First notice that, due to the symmetry of the lattice, the DMI contribution is annulled, and the only nonzero term of SIA matrix is \mathcal{A}^{zz} ,²⁰ such that the SIA contribution to the energy of the i^{th} spin becomes $\mathcal{A}^{zz}(S_i^z)^2$. Assuming that both CrBr₃ and CrI₃ have strong out-of-plane anisotropy, the exchange energy can be rewritten in terms of an isotropic exchange $J_0 = \langle J^{xx} \rangle$, and the anisotropic term $\Delta = \langle J^{zz} \rangle - \langle J^{xx} \rangle$, where $\langle \dots \rangle$ represents the average over the three nearest-neighbour pairs. The lattice symmetry guarantees that $\langle J^{yy} \rangle = \langle J^{xx} \rangle = J_0$ and $\langle J^{ab} \rangle = 0$ for $a \neq b$ [see, e.g., Table I]. The Hamiltonian for the i^{th} spin takes the simple form of the XXZ model^{11,32,33}

$$\mathcal{H}_i = J_0 \sum_j \mathbf{S}_i \cdot \mathbf{S}_j + \Delta \sum_j S_i^z S_j^z + \mathcal{A}^{zz} (S_i^z)^2, \quad (4)$$

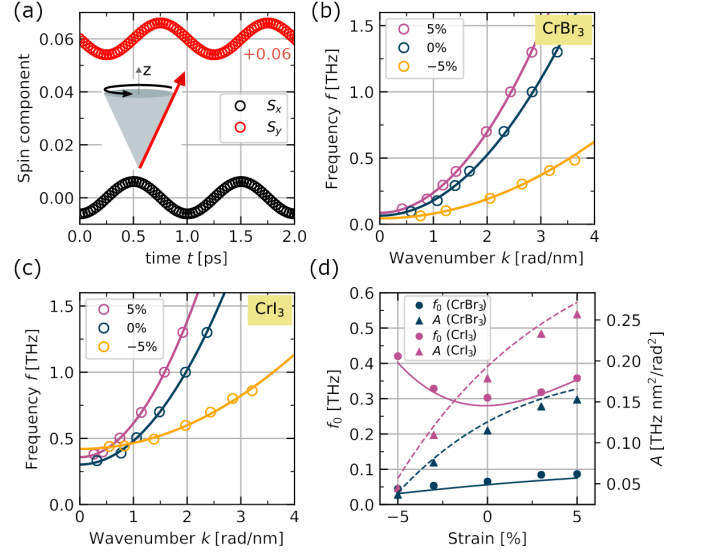


FIG. 2. (a) Temporal evolution of the spin components for the case of a 1 THz spin wave. The S_y spin component is vertically shifted for better visualization. (b,c) Spin-wave dispersion relation obtained in the simulations for CrBr₃ (b) and CrI₃ (c), under different strain. Solid lines show the numerical fit to the quadratic expression $f(k) = Ak^2 + f_0$. (d) The values of the fitted parameters A and f_0 obtained as a function of strain. Solid and dashed lines are the analytical expressions (obtained from Eq. (5)) for f_0 and A , respectively.

where the sum in j runs over the three nearest-neighbours of the i^{th} spin. The SW dispersion is then calculated by assuming the linearized solution $\hat{S}^z \approx 1$, $\hat{S}^x \approx A_0 e^{i(\mathbf{k}\cdot\mathbf{r}-\omega t)}$ and $\hat{S}^y \approx iA_0 e^{i(\mathbf{k}\cdot\mathbf{r}-\omega t)}$, where $A_0 \ll 1$ represents the SW amplitude; ω is the SW angular frequency and \mathbf{r} is the position of the considered spin. Substituting that into the LLG equation [Eq. (3)], with the effective field derived from Eq. (4), we obtain²⁶

$$\omega(k) = \frac{\gamma S^2}{(1 + \alpha^2)\mu} [3\Delta + 2\mathcal{A}^{zz} + J_0 g(\mathbf{k})], \quad (5)$$

with

$$g(\mathbf{k}) = 3 - \cos(ka) - 2 \cos(ka/2), \quad \text{if } \mathbf{k} \parallel \hat{\mathbf{n}}_1, \quad (6)$$

$$g(\mathbf{k}) = 2 - 2 \cos(ka\sqrt{3}/2), \quad \text{if } \mathbf{k} \parallel \hat{\mathbf{n}}_2,$$

where a is the distance between nearest-neighbour pairs, and $\hat{\mathbf{n}}_1$ and $\hat{\mathbf{n}}_2$ are the main symmetry axis of the honeycomb lattice, as shown in Fig. 1.

Notice that in the limit of small ka Eq. (6) can be approximated as $g(\mathbf{k}) \approx \frac{3a^2}{4}k^2$ for both $\mathbf{k} \parallel \hat{\mathbf{n}}_1$ and $\mathbf{k} \parallel \hat{\mathbf{n}}_2$. The SW frequency $f = \omega/2\pi$ then assumes quadratic dependence on the wavenumber k . The solid and dashed lines in Fig. 2(d) show the analytical solutions (with $\alpha^2 \ll 1$) for the zero-momentum SW frequency $f_0 = \frac{\gamma S^2}{2\pi\mu}(3\Delta + 2\mathcal{A}^{zz})$ and the quadratic coefficient $A = \frac{\gamma S^2}{2\pi\mu} \frac{3a^2 J_0}{4}$, respectively, which are in very good agreement with the numbers obtained in the simulations.

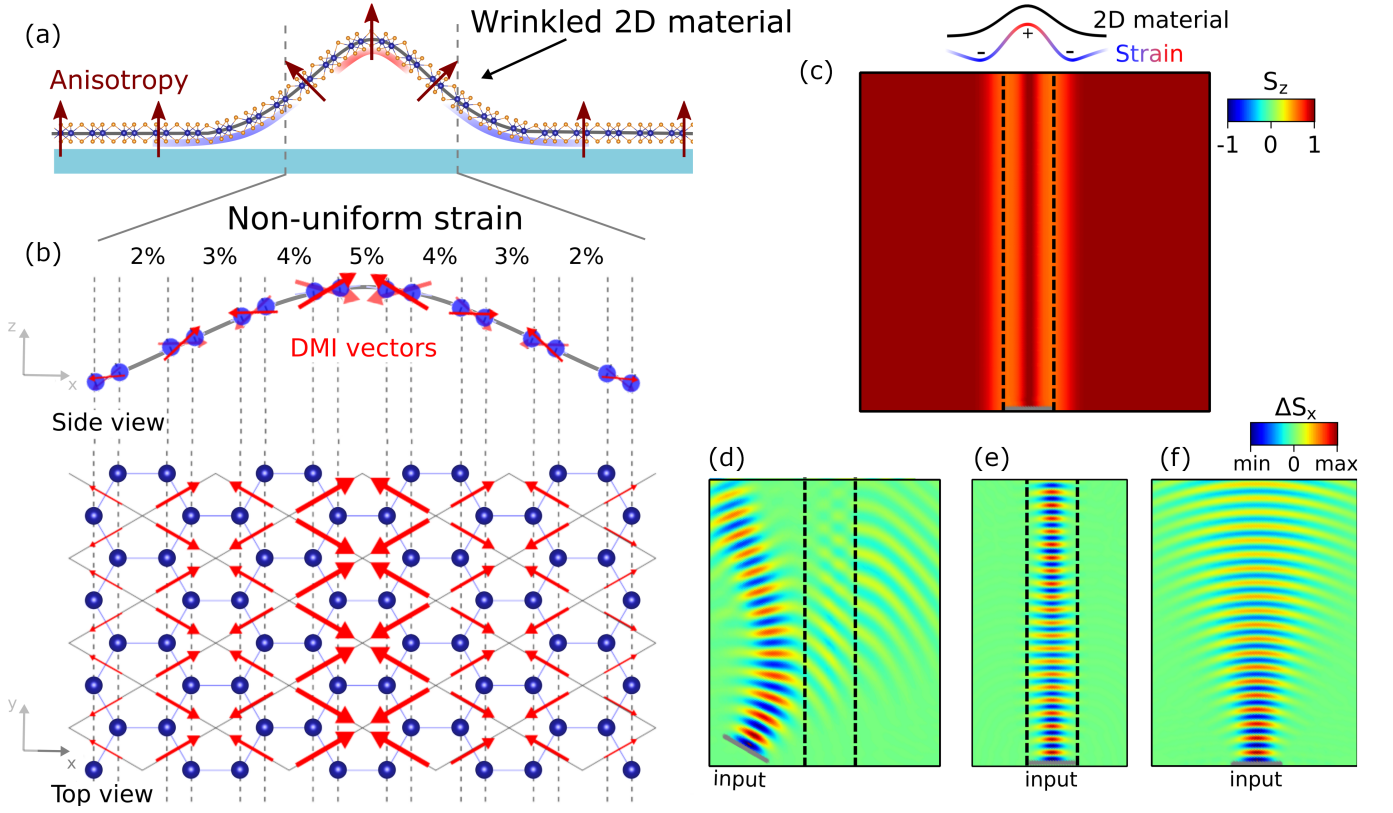


FIG. 3. (a) Schematic view of a wrinkled 2D magnetic material. The induced curvature is nonuniformly straining the 2D material, while the magnetic anisotropy remains orthogonal to the monolayer surface. Here, the red shade shows tensile strain and the blue shade represents the compressive strain. (b) Illustration of the DMI pattern expected in the case of nonuniform strain in the CrX_3 monolayer¹⁶. (c) Snapshot of the simulated magnetic ground state around a wrinkle in the 2D material. Dashed lines indicate the maximal vertical slope in the 2D material. (d-e) Snapshots of simulated SW propagation (d) across and (e) along a wrinkle in CrI_3 , with $f = 0.5$ THz. (f) Snapshot of the SW simulation corresponding to (e), but for pristine (flat) monolayer.

The values of Δ , A^{zz} and J_0 as a function of strain are shown in Fig. S1 of the supplemental material²⁶. One thus concludes that the XXZ model [Eq. (4)] is a suitable approximation to describe properties of SWs in uniform CrI_3 and CrBr_3 2D magnets.

In the case where the CrX_3 lattice experiences non-zero DMI, such as in Janus structures¹³ or in the presence of out-of-plane applied electric field^{14,15}, the linearized solution for the SW dispersion [Eq. (5)] results in an extra term that has linear dependence on the wavevector k .³⁴ The contribution of DMI to the SW dispersion depends on the angle between the DMI vector and the axis around which the spins rotate, and the strongest effect is observed when the magnetization lies in the same plane as the DMI vectors. Details on the calculation of SW dispersion in presence of uniform DMI are provided in the supplemental material²⁶.

4. Flexo-magnonics

The strong response of SW properties to strain in the 2D material suggests the possibility of flexo-magnonic applications. In fact, 2D materials are mostly very flexi-

ble and can be strain engineered in a multitude of ways. For example, localized strain can be induced by growing the 2D material on top of a patterned substrate^{35,36}, or by placing it onto elastometric or piezoelectric substrate, whose compression may lead to wrinkling and buckling of the 2D material³⁶⁻³⁸. In addition, bubbles and tents can be formed in the 2D material by trapping water, gas or solid nanoparticles at the interface between the magnetic monolayer and the substrate^{39,40}.

To exemplify the interaction of SWs with such localized heterostrained structures we simulate the interaction of a propagating SW with a wrinkle in the CrI_3 monolayer. Fig. 3(a) illustrates the considered system. In such a configuration, the position of a generic Cr atom in the curved monolayer can be parametrized as $\mathbf{r}' = \mathbf{r} + \mathbf{u}(\mathbf{r})$, where $\mathbf{r} = (x, y, 0)$ is the atom position in the pristine (flat) lattice and $\mathbf{u}(\mathbf{r}) = (u_x(\mathbf{r}), u_y(\mathbf{r}), h(\mathbf{r}))$ the position displacement. Here, u_x and u_y represent the in-plane displacement and $h(\mathbf{r})$ is a scalar field accounting for out-of-plane deformations. The red and blue shades in Fig. 3 (a) illustrate the expected regions of tensile and compressive strain respectively⁴¹. In addition to the local

strain, the curvature also induces a rotation in the direction of the magnetic anisotropy, which points orthogonal to the surface of the magnetic film [Fig. 3(a)]. Moreover, due to the non-uniform deformation, the corresponding symmetry-breaking gives rise to localized DMI¹⁶. Figure 3(b) illustrates the expected DMI configuration in the case of a non-uniform uniaxial strain in the wrinkled CrX₃ monolayer. DFT calculations show that the DMI increases linearly with local uniaxial strain, with relatively small magnitude of up to $D = 0.08$ meV for 6% of local strain¹⁶.

First-principles calculations of such a curved structure are very challenging, requiring relaxation of the atomic structure over a large area before calculating locally the magnetic parameters for a number of distinctly different Cr-Cr pairs due to heterostrain. Instead, as a first step in understanding the interaction of SWs in such systems, here we model the material curvature by rotating the local bases of eigenvectors of the magnetic Hamiltonian [Eq. (2)] accordingly to the surface normal, and vary the magnitude of interactions accordingly to the local strain profile of the curvature. Note that the considered magnetic Hamiltonian is completely determined by the exchange and anisotropy matrices and the angle between neighbouring spins, therefore, local deformations can be modeled by correspondingly modifying the interaction matrices and precise atomic positions do not play a role. Fig. 3(c) shows the magnetic ground state obtained in such simulations for a single wrinkle of Gaussian shape $h(\mathbf{r}) = h_0 e^{-\frac{x^2}{w^2}}$, where $h_0 = 20$ nm and $w = 15$ nm define the height and width of the wrinkle, respectively. The considered strain profile has maximal deformation of $\epsilon = 5\%$ on top of the wrinkle⁴¹⁻⁴³ and satisfies $\epsilon(x) \propto \partial^2 h(\mathbf{r})/\partial x^2$. Notice that the curvature induces local canting in the ground-state magnetization and increases spin-stiffness due to emergent DMI. Fig. 3(d-f) shows snapshots of the simulated propagation of a 0.5 THz SW (d) across and (e) along the wrinkle, where the SW can either be reflected by or confined along the flexed region, respectively, in comparison with the case of a pristine (flat) sample (f). Recalling the wide range of possibilities for nanoengineered manipulation of 2D materials, this basic example suffices to promote ideas towards flexo-magnonic applications.

5. Scattering of spin-waves on lattice defects

Vacancies are the most commonly observed defect in 2D materials. They are not only an unwanted product of synthesis or manipulation of the sample, but can also be deliberately artificially induced by vacancy engineering^{44,45}. In this section we therefore investigate the interaction of SWs with such defects (halides vacancies) in CrX₃ lattice. The local breaking of the inversion symmetry seen by Cr atoms in the vicinity of the lattice defect results in appearance of DMI, as shown in Fig.4(a). It is well known that SWs are strongly affected

by the DMI interaction and can even be controllably refracted/reflected at an interface where DMI changes^{46,47}. In the case of lattice defects, *ab initio* calculations reveal DMI vectors of magnitudes up to $D = 4.69$ meV for CrI₃ and $D = 2.60$ meV for CrBr₃ in the vicinity of halide vacancies¹⁶. One thus expects pronounced effects of such strong variations of the local magnetic interactions on the SW propagation in the 2D magnetic materials.

To start with, we consider the scattering of SWs in CrBr₃ and CrI₃ with different density of randomly distributed halide vacancies η (density expressed as the number of vacancies per Cr atom). The used magnetic parameters, as obtained from first-principles calculations, are listed in Table II and in the supplemental material²⁶. Fig. 4(b-d) shows the snapshots of simulated SW propagation through the CrI₃ monolayer for $\eta = 0, 0.01$ and 0.02 , respectively. The corresponding output SW amplitudes, measured at a distance of 100 nm from the SW source [Fig.4 (e-g)], reveal that the transmitted wave is strongly affected in the case of high density of defects. In order to quantify and compare the SW transmission for different defect densities, we integrate the output SW

Isolated defect					
	pair (<i>i-j</i>)	D^x (meV)	D^y (meV)	D^z (meV)	$ D $ (meV)
CrI ₃	(1-2)	0.29	-0.20	-0.53	0.64
	(2-3)	4.05	-2.33	-0.39	4.69
	(2-5)	0.17	0.09	-0.46	0.50
	(3-4)	0.01	0.11	-0.06	0.12
	(3-6)	0.01	-0.38	0.19	0.42
CrBr ₃	(1-2)	-0.05	-0.13	0.26	0.29
	(2-3)	2.24	-1.31	-0.08	2.60
	(2-5)	0.00	0.06	-0.04	0.07
	(3-4)	0.02	0.03	0.07	0.08
	(3-6)	-0.09	-0.14	0.07	0.18
Line of defects					
	pair (<i>i-j</i>)	D^x (meV)	D^y (meV)	D^z (meV)	$ D $ (meV)
CrI ₃	(1-2)	0.01	-0.43	0.06	0.44
	(2-3)	-0.05	-0.55	2.42	2.48
	(2-5)	3.61	-0.27	4.23	5.57
	(3-4)	-0.09	0.03	-0.23	0.25
	(3-6)	3.61	-0.27	4.23	5.57
CrBr ₃	(1-2)	0.00	-0.09	0.01	0.09
	(2-3)	0.12	0.14	0.47	0.50
	(2-5)	2.09	-0.02	1.50	2.57
	(3-4)	-0.04	-0.03	0.01	0.05
	(3-6)	2.09	-0.02	1.50	2.57

TABLE II. Induced DMI parameters at an isolated defect (halide vacancy) and at a line of such defects in CrI₃ and CrBr₃, obtained from first-principle calculations¹⁶. The complete exchange matrix for both cases is provided in the supplemental material²⁶. Pairs (*i-j*) are indicated in Fig. 4 (a) and Fig. 6 (a).

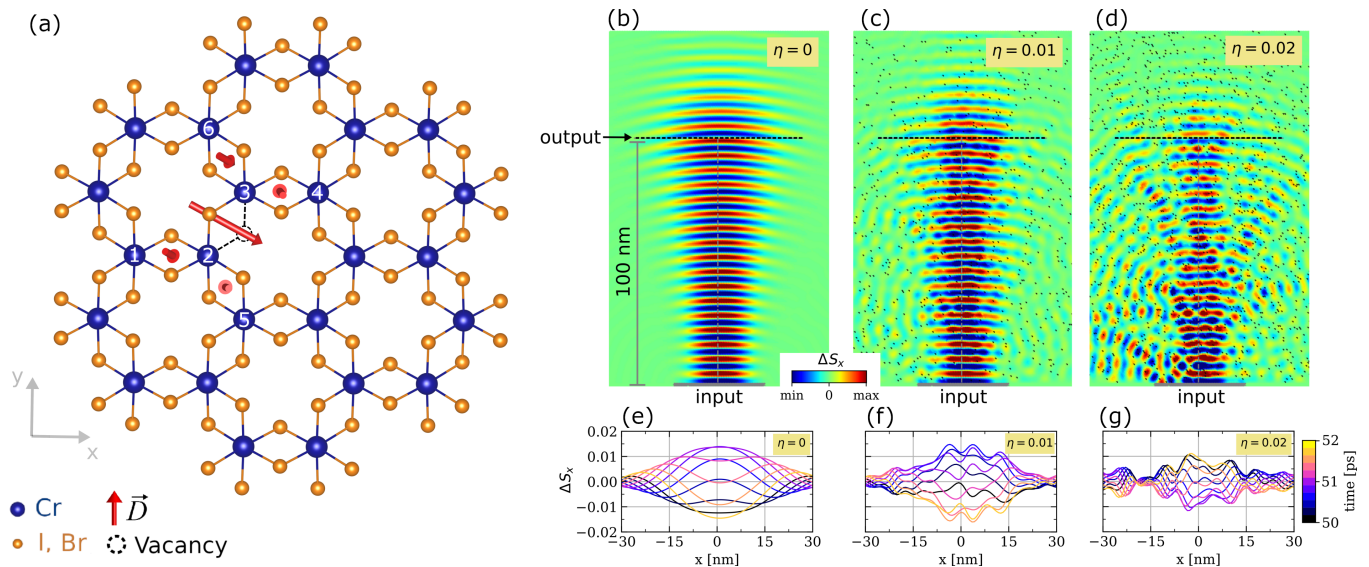


FIG. 4. (a) CrX_3 lattice in the vicinity of a single halide vacancy. Induced DMI vectors are shown as red arrows. (b-d) Snapshots of simulated SW propagation in presence of randomly distributed defects in CrI_3 , for defect densities $\eta = 0$, $\eta = 0.01$, $\eta = 0.02$ vacancies per Cr atom, respectively. The input SW frequency is 0.5 THz. (e-g) Corresponding output SW amplitudes for the cases shown in (b-d), respectively, measured at a distance of 100 nm from the SW source. Colors in (e-g) correspond to different time instances during the 2 ps SW period.

amplitudes along the direction perpendicular to the SW propagation and normalize it with respect to the case without defects, i.e., for $\eta = 0$. Fig. 5 (a) shows such normalized transmission for the 0.5 THz SWs in CrBr_3 and CrI_3 . Notice that SWs in CrI_3 are more affected by the halide vacancies when compared to CrBr_3 . We relate this property to the large DMI interactions induced in CrI_3 , which are approximately twice as large as in the CrBr_3 sample, predominantly due to stronger spin-orbit coupling on iodine compared to bromine.

Scattering on defects, as shown in Fig. 4, especially over large distances, must clearly be taken into account when designing novel magnonic devices based on 2D ma-

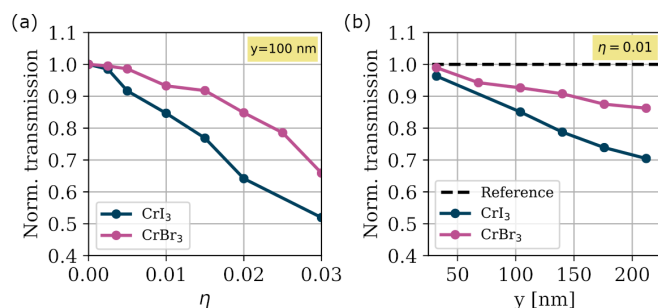


FIG. 5. (a) The normalized transmission of SWs as a function of the density of defects, η , measured at a distance of $y = 100$ nm from the SW source, with $f = 0.5$ THz. (b) SW transmission as a function of the distance to the output, for $\eta = 0.01$ and $f = 0.5$ THz. Here, the transmission amplitudes are normalized with respect to the case of $\eta = 0$, measured at the same distance from the SW source.

terials. Therefore in Fig. 5(b) we show the SW transmission as a function of the output distance, normalized with respect to the case of $\eta = 0$, measured at the same distance from the SW source. Notice that the normalized transmission decreases quasi-linearly as a function of the output distance, where the transmission in CrI_3 decreases at approximately twice higher rate than in CrBr_3 , for $\eta = 0.01$, thus again reflecting the stronger response of SWs to defects in CrI_3 . Finally we note that we have not observed any significant frequency dependence (for the range of 0.3 to 1.5 THz) in the results presented in this section.

5.1. Defect-engineering of magnonic circuitry

As demonstrated above, the induced strong variations in magnetic parameters around the lattice defects strongly affect the SW propagation. Therefore, a designed pattern of defects, such as a chain of adjacent defects, may be able to e.g. confine the SWs and serve as a waveguide. To illustrate this point, we investigate the interaction of SWs with a row of consecutive halide vacancies in CrX_3 lattices, as a possible way of controlling the SW propagation direction in magnetic 2D materials.

The emergent DMI in the considered structure, as illustrated in Fig. 6(a), is similar in magnitude to DMI found in the vicinity of isolated defects. The exact values are listed in Table II for comparison, while complete exchange matrices are provided in the supplemental material²⁶. Fig. 6(b) shows a snapshot of the simulation for a SW directed across the defect line in CrI_3 , where we consider a 0.5 THz SW reaching the defect line under an incident angle of $\phi = \pi/4$. Notice that only a small fraction of the SW is able to cross the defect line while

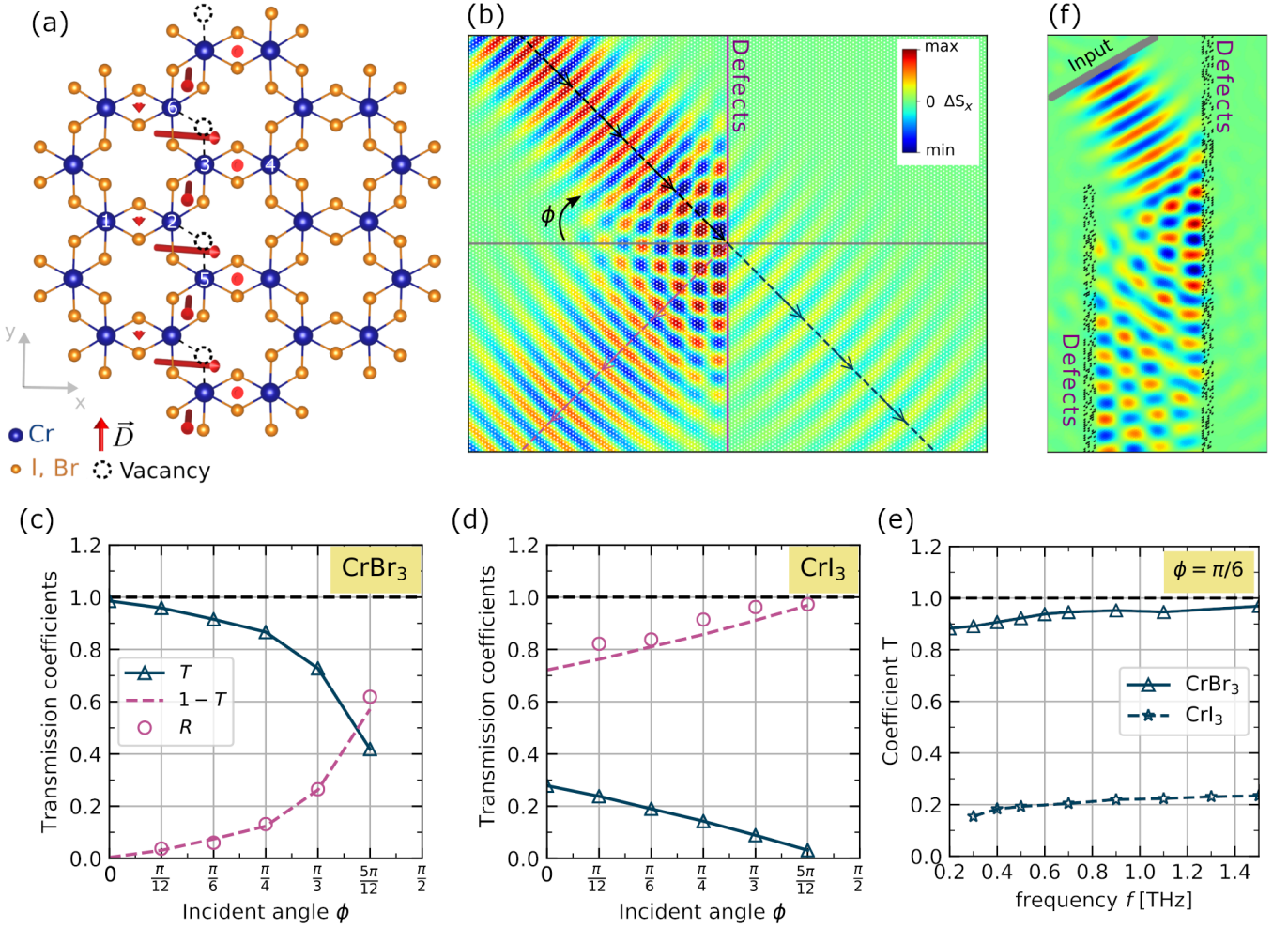


FIG. 6. (a) CrX_3 lattice with a line of halides vacancies. Induced DMI vectors are illustrated as red arrows. (b) Reflection of a SW by a defect line shown in (a). Snapshot captures a spin-wave of frequency 0.5 THz reaching the defect line in CrI_3 under an incident angle of $\phi = \pi/4$. Arrows indicate the SW propagation direction. (c-d) Transmission and reflection coefficients as a function of the incident angle ϕ for CrBr_3 (c) and CrI_3 (d), obtained for SW frequency $f = 0.5$ THz and damping $\alpha = 0.001$. (e) Frequency dependence of the transmission coefficient T for both CrBr_3 and CrI_3 at fixed incident angle $\phi = \pi/6$. (f) Snapshot of the simulations for the SW confinement between two realistically broadened defect lines in the magnetic 2D material.

the major part is reflected. In Fig. 6(c-d) we show the transmission coefficients, defined as^{48,49}

$$T = \left(\frac{\Delta_T}{\Delta_0} \right)^2, R = \left(\frac{\Delta_R}{\Delta_0} \right)^2, \quad (7)$$

where Δ_T and Δ_R are the amplitudes of the transmitted and reflected waves, respectively, and Δ_0 is the corresponding SW amplitude in the absence of defects, calculated at the same distance from the SW source. The reflection and transmission coefficients are defined to satisfy the relation $R = 1 - T$. In Fig. 6(c-d) the transmission and reflection coefficients are shown as a function of incident angle ϕ for CrBr_3 [Fig. 6(c)] and CrI_3 [Fig. 6(d)]. Notice that SWs experience stronger reflection by the defect line in CrI_3 while most part of the SW is transmitted across the vacancy defect line in CrBr_3 . Once again we relate this property to the larger DMI induced at defects

in CrI_3 . Similar to an interface where DMI changes⁴⁶, the reflection is enhanced with increasing the incident angle from $\phi = 0$ towards $\phi = \pi/2$. However, total reflection is not found in our simulations, which is due to a finite cross-talk of spins on two sides of the defect line, where DMI is not present, which is different in the case of a DMI interface. Fig. 6(e) shows the frequency dependence of the transmission coefficient T for both CrBr_3 and CrI_3 for a fixed incident angle $\phi = \pi/6$, which shows a weak increase of transmission with increasing SW frequency.

Of course, such a precise pattern of defects is unlikely to be reproduced experimentally by vacancy engineering in a 2D material^{44,45}. However, a broadened defective region can also be made useful in a similar sense, even if induced by e.g. low-energy electron-beam⁴⁴ or by “scratching” the material with a scanning tip. To illustrate such a case, in Fig. 6(f) we show the snapshot of the simula-

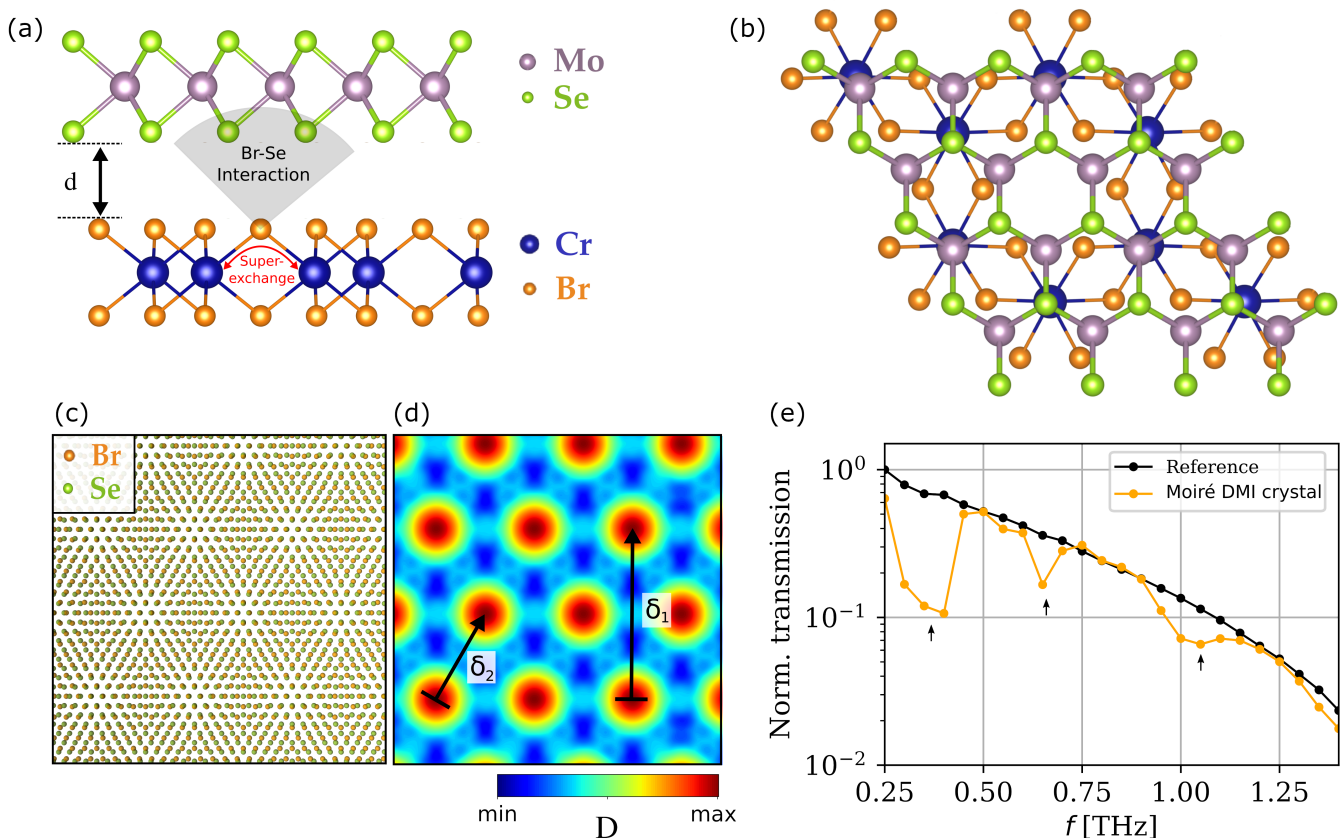


FIG. 7. Example of a moiré magnonic crystal. (a-b) Illustration of a $\text{CrBr}_3/\text{MoSe}_2$ vdW heterobilayer, viewed from the side (a) and the top (b). (c) moiré pattern created between adjacent Br and Se sublayers. (d) Corresponding DMI profile emerging in the Cr sublayer from the moiré pattern shown in (c). Here, δ_1 and δ_2 denote the two main periodicities of the system. (e) Simulated SW transmission spectra after passing through the moiré magnonic crystal (with maximal DMI of 3 meV), in comparison with the reference waveguide (pristine film), where we consider the incident SW propagating along the δ_1 direction. Black arrows indicate the critical frequencies where SWs suffer destructive interference.

tion for the SW propagating in CrI_3 , across a distribution of defects, randomly placed along 5 nm wide stripes, roughly mimicking surface scratches on the magnetic 2D material. Notice that such a pattern of defects can also confine the SWs, and can be engineered to (de)stimulate self-interference patterns, or control interactions of two incoming spin-waves. The key ingredient for confining and controlling the SWs remains the local variation of the magnetic parameters, which can also be induced by electric gating¹⁴ or strain-engineering the 2D material, as demonstrated in Sec. 4, albeit on a significantly larger scale than what is offered by defect engineering.

6. Moiré van der Waals magnonic crystals

Magnonic crystals are artificial materials designed in such a way that the magnetic properties of the media are characterized by a periodic lateral variation¹⁹. The SW spectra in such materials exhibit features such as band gaps of wavelengths that are not allowed to propagate, which is useful for magnonic filters as well as information transport and processing based on magnons. Periodic variations of the magnetic parameters in the 2D

magnetic materials can be induced in multiple ways, for example, by periodic electric gating⁵⁰, strain engineering^{36,38,40}, by growing the 2D material on top of a patterned substrate³⁵, or by inducing a checkerboard buckling of the monolayer⁵¹. However, a magnonic crystal for THz frequencies requires a modulation period of just a few nanometers²⁹ [see SW dispersion relation in Fig. 2], which is beyond the ability of the fabrication methods mentioned above. Instead, we propose here to employ a moiré pattern in a van der Waals (vdW) heterobilayer as the source of the periodic modulation in magnetic parameters for the design of magnonic crystals in the high-frequency regime. It is readily established that a moiré pattern can induce periodic variation in the magnetic parameters of a 2D material^{17,18}. Therefore, let us consider the case where the CrX_3 monolayer is stacked on top of another, non-magnetic material, in order to produce a moiré pattern. For instance, we consider the vdW heterobilayer $\text{CrBr}_3\text{-MoSe}_2$, as illustrated in Fig. 7(a,b). The superexchange interaction between Cr atoms, mediated by the Cr-Br-Cr bonds, will be affected by the Br-Se interaction at the interface between monolayer constituents

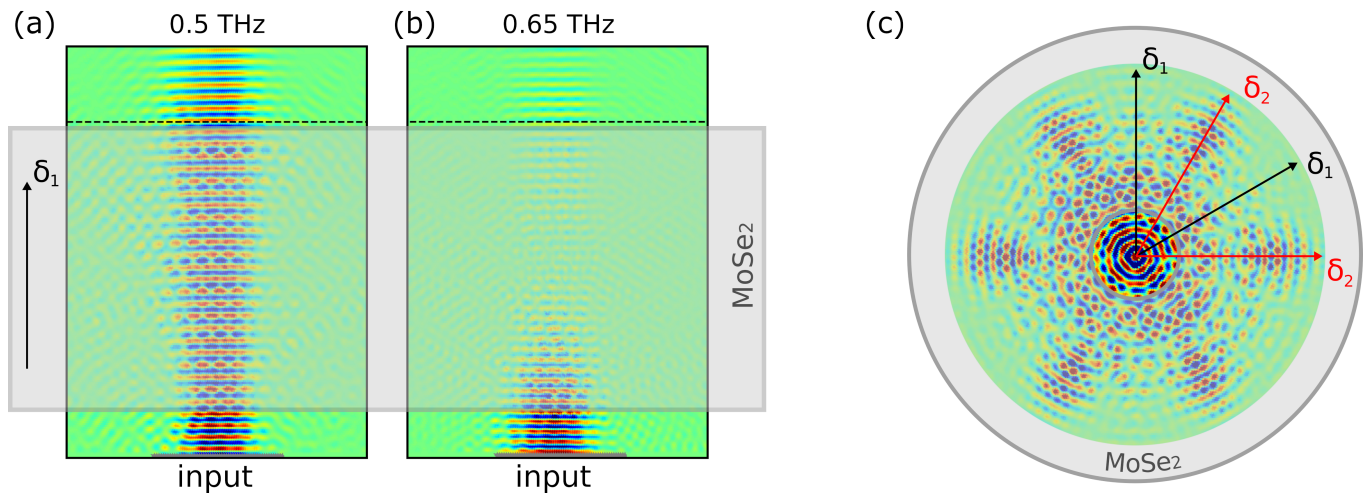


FIG. 8. (a-b) Snapshots of SW simulation for the 0.5 and 0.65 THz SWs propagating across the moiré pattern for the same period of time. The incident SW propagates parallel to the δ_1 direction. (c) Snapshots of the SW simulation for the 0.4 THz SW propagating across the moiré pattern, after being emitted in a radially symmetric fashion from a point source. SW propagation is clearly prohibited along the δ_1 directions, but remains enabled along the δ_2 direction.

of the heterobilayer, which in turn varies with the local stacking throughout the moiré pattern. In other words, the periodicity of the moiré structure is directly reflected in a periodic modulation of the resultant magnetic parameters. Fig. 7(c) shows the moiré pattern created between the Br sublayer (a trigonal lattice with lattice constant $a_{\text{Br}} = 3.698 \text{ \AA}$) and the Se sublayer (a trigonal lattice with lattice constant $a_{\text{Se}} = 3.289 \text{ \AA}$)⁵². Here the symmetry axes of the two lattices are considered to be aligned, which corresponds to an angle of 30° between CrBr_3 and MoSe_2 supercells⁵³. The mismatch in the lattice constants creates the moiré pattern with two characteristic periodicities of $\delta_1 \approx 5.13 \text{ nm}$ and $\delta_2 \approx 2.96 \text{ nm}$, as indicated in Fig. 7(d). Such short periodicities found in the moiré heterostructures are, therefore, capable of interacting with high frequency SWs and can be adjusted, for example, by fine interlayer twisting, or replacing the MoSe_2 layer with a 2D material with a different lattice constant and/or different lattice symmetry.

Therefore, in the present case the interaction between Br and Se atoms breaks the inversion symmetry seen by the Cr sublayer where magnetism resides, and significantly affects the superexchange owing to the strong spin-orbit coupling in MoSe_2 ^{54,55}. As a result, one can expect a periodic modulation in the DMI parameter throughout the magnetic layer, directly mapped on the moiré pattern between Br and Se sublayers. As a first step in understanding the magnonics in such a complex system, and considering that DMI has the main impact on SWs, we will consider a moiré periodic modulation only in the DMI parameter, and assume the other magnetic parameters in CrX_3 monolayer remain unchanged by vdW heterostructuring. Fig. 7(d) shows the used DMI profile, reflecting the moiré pattern, according to the expression $D = D_0 \exp(-\sqrt{r^2 + d^2}/r_0)$, where r is the lateral distance between Br and Se atoms, $d = 3.5 \text{ \AA}$ is the separa-

tion between the layers⁵³ [see Fig. 7 (a)] and D_0 and r_0 are constants that define the DMI magnitude. Here we consider $D_0 = 3 \exp(d/r_0) \text{ meV}$ and $r_0 = 0.2 \text{ \AA}$, such that the maximum magnitude of DMI is 3 meV. The small value of r_0 reflects the short range interaction between neighbouring orbitals, such that the maximal interaction is given when Se atoms are on top of Br ones. Notice that a SW propagating in such a system will experience different periodic modulations, depending on the propagation direction, with respect to the two main periodicities in the system δ_1 and δ_2 [cf. Fig. 7(d)].

Fig. 7(e) shows the simulated SW transmission spectrum of the moiré magnonic crystal described above, in comparison with the reference waveguide (pristine CrBr_3 monolayer), where we considered the incident SW propagating parallel to the δ_1 direction. Notice that the transmission spectrum of the moiré system significantly differs from the pristine medium, as three distinct valleys of prohibited magnon frequencies are visible. Such a spectrum is typical of magnonic crystals¹⁹. Fig. 8(a-b) shows the snapshots of SW simulation for the 0.5 and 0.65 THz SWs propagating across the moiré DMI pattern, where in the latter case the SWs suffer destructive interference and do not propagate.

Finally, one notices that the hexagonal symmetry in the modulation of magnetic parameters results in the anisotropic dispersion of the spin waves. Fig. 8(c) shows the snapshots of SW simulation for the 0.4 THz SW emitted radially across the moiré pattern, from a point source. In this case, SW propagation is effectively blocked along the δ_1 directions, as expected from the transmission spectra in Fig. 7(e), but remains enabled along the δ_2 directions – demonstrating the anisotropic SW dispersion characteristic of moiré magnonic systems.

7. Conclusions

In summary, we presented an overview of magnonic properties in monolayer chromium trihalides CrBr₃ and CrI₃, including selected possibilities for tuning the magnonic behavior in these and similar magnetic 2D materials. We revealed that the spin-wave (SW) dispersion relation can be tuned in a broad range of frequencies by straining the 2D magnetic monolayer, and that the SW dispersion has different response to strain in CrBr₃ compared to CrI₃, which is directly related to differences in their out-of-plane anisotropy. We further demonstrated the possibility of controlling the SW propagation by strain-engineering the 2D material, paving the way towards flexo-magnonic applications. As a next step, we discussed the effect of ever-present structural defects (in this case halide vacancies) on SW propagation in chromium trihalide monolayers. Our calculations show that such lattice defects induce sufficiently large DMI to strongly disturb the SW dynamics, especially in CrI₃. However, we also show that a pattern of defects can be designed favorably for magnonic circuitry, as extended defect lines are able to confine SWs and may be useful for SW-guides.

Finally, we discuss the spectra of SWs propagating across periodic modulation of the magnetic parameters, induced by a moiré pattern in a van der Waals heterobilayer of a magnetic and a non-magnetic 2D material. Such moiré heterostructures exhibit the necessary nanoscale modulation period to work as a magnonic crystal for the terahertz SWs characteristic for CrX₃ monolayers. Even though we presented only a small fraction of possible manipulations of 2D materials, their pronounced impact on local magnetism and spin excitations, facilitated heterostructuring, as well as the ease of employing additional electronic gating and nanolithography in any desired geometry, promotes magnetic 2D materials to the prime echelon of candidates for terahertz magnonics by design.

Acknowledgements

This work was supported by the Research Foundation - Flanders (FWO-Vlaanderen), the Special Research Funds of the University of Antwerp (BOF-UA), and Brazilian agencies FACEPE, CAPES and CNPq.

* milorad.milosevic@uantwerpen.be

- ¹ C. Bacaksiz, D. Šabani, R. M. Menezes, and M. V. Milošević, “Distinctive magnetic properties of CrI₃ and CrBr₃ monolayers caused by spin-orbit coupling,” *Physical Review B* **103**, 125418 (2021).
- ² S. I. Vishkayi, Z. Torbatian, A. Qaiumzadeh, and R. Asgari, “Strain and electric-field control of spin-spin interactions in monolayer CrI₃,” *Physical Review Materials* **4**, 094004 (2020).
- ³ B. Huang, G. Clark, D. R. Klein, D. MacNeill, E. Navarro-Moratalla, K. L. Seyler, N. Wilson, M. A. McGuire, D. H. Cobden, D. Xiao, *et al.*, “Electrical control of 2D magnetism in bilayer CrI₃,” *Nature Nanotechnology* **13**, 544–548 (2018).
- ⁴ S. Jiang, L. Li, Z. Wang, K. F. Mak, and J. Shan, “Controlling magnetism in 2D CrI₃ by electrostatic doping,” *Nature nanotechnology* **13**, 549–553 (2018).
- ⁵ W. Chen, Z. Sun, Z. Wang, L. Gu, X. Xu, S. Wu, and C. Gao, “Direct observation of van der waals stacking-dependent interlayer magnetism,” *Science* **366**, 983–987 (2019).
- ⁶ N. Sivadas, S. Okamoto, X. Xu, C. J. Fennie, and D. Xiao, “Stacking-dependent magnetism in bilayer CrI₃,” *Nano Letters* **18**, 7658–7664 (2018).
- ⁷ J. Shang, X. Tang, X. Tan, A. Du, T. Liao, S. C. Smith, Y. Gu, C. Li, and L. Kou, “Stacking-dependent interlayer magnetic coupling in 2d CrI₃/CrGeTe₃ nanostructures for spintronics,” *ACS Applied Nano Materials* **3**, 1282–1288 (2019).
- ⁸ C. Gong and X. Zhang, “Two-dimensional magnetic crystals and emergent heterostructure devices,” *Science* **363** (2019).
- ⁹ J. Cenker, B. Huang, N. Suri, P. Thijssen, A. Miller, T. Song, T. Taniguchi, K. Watanabe, M. A. McGuire, Di. Xiao, *et al.*, “Direct observation of two-dimensional magnons in atomically thin CrI₃,” *Nature Physics* **17**, 20–25 (2021).
- ¹⁰ W. Jin, H. Ho Kim, Z. Ye, S. Li, P. Rezaie, F. Diaz, S. Siddiq, E. Wauer, B. Yang, C. Li, *et al.*, “Raman fingerprint of two terahertz spin wave branches in a two-dimensional honeycomb ising ferromagnet,” *Nature communications* **9**, 1–7 (2018).
- ¹¹ J. L. Lado and J. Fernández-Rossier, “On the origin of magnetic anisotropy in two dimensional CrI₃,” *2D Materials* **4**, 035002 (2017).
- ¹² C. Xu, J. Feng, H. Xiang, and L. Bellaiche, “Interplay between kitaev interaction and single ion anisotropy in ferromagnetic CrI₃ and CrGeTe₃ monolayers,” *npj Computational Materials* **4**, 1–6 (2018).
- ¹³ C. Xu, J. Feng, S. Prokhorenko, Y. Nahas, H. Xiang, and L. Bellaiche, “Topological spin texture in janus monolayers of the chromium trihalides Cr (I, X)₃,” *Physical Review B* **101**, 060404 (2020).
- ¹⁴ J. Liu, M. Shi, J. Lu, and M. P. Anantram, “Analysis of electrical-field-dependent dzyaloshinskii-moriya interaction and magnetocrystalline anisotropy in a two-dimensional ferromagnetic monolayer,” *Physical Review B* **97**, 054416 (2018).
- ¹⁵ A. K. Behera, S. Chowdhury, and S. R. Das, “Magnetic skyrmions in atomic thin CrI₃ monolayer,” *Applied Physics Letters* **114**, 232402 (2019).
- ¹⁶ D. Sabani, C. Bacaksiz, and M. V. Milosevic, “Releasing latent chirality in magnetic two-dimensional materials,” *arXiv preprint arXiv:2009.03421* (2020).
- ¹⁷ F. Xiao, K. Chen, and Q. Tong, “Magnetization textures in twisted bilayer CrX₃ (X= Br, I),” *Physical Review Research* **3**, 013027 (2021).

- ¹⁸ Q. Tong, F. Liu, J. Xiao, and W. Yao, “Skyrmions in the moiré of van der waals 2d magnets,” *Nano Letters* **18**, 7194–7199 (2018).
- ¹⁹ A. V. Chumak, A. A. Serga, and B. Hillebrands, “Magnonic crystals for data processing,” *Journal of Physics D: Applied Physics* **50**, 244001 (2017).
- ²⁰ D. Šabani, C. Bacaksiz, and M. V. Milošević, “Ab initio methodology for magnetic exchange parameters: Generic four-state energy mapping onto a heisenberg spin hamiltonian,” *Physical Review B* **102**, 014457 (2020).
- ²¹ M. A. McGuire, H. Dixit, V. R. Cooper, and B. C. Sales, “Coupling of crystal structure and magnetism in the layered, ferromagnetic insulator CrI_3 ,” *Chemistry of Materials* **27**, 612–620 (2015).
- ²² M. Kim, P. Kumaravel, J. Birkbeck, W. Kuang, S. G. Xu, D. G. Hopkinson, J. Knolle, P. A. McClarty, A. I. Berdyugin, M. B. Shalom, *et al.*, “Micromagnetometry of two-dimensional ferromagnets,” *Nature Electronics* **2**, 457–463 (2019).
- ²³ G. P. Müller, M. Hoffmann, C. Dißelkamp, D. Schürhoff, S. Mavros, M. Sallermann, N. S. Kiselev, H. Jönsson, and S. Blügel, “Spirit: Multifunctional framework for atomistic spin simulations,” *Physical Review B* **99**, 224414 (2019).
- ²⁴ P. Gruszecki, M. Kasprzak, A. E. Serebryannikov, M. Krawczyk, and W. Śmigaj, “Microwave excitation of spin wave beams in thin ferromagnetic films,” *Scientific Reports* **6**, 1–8 (2016).
- ²⁵ M. Song, K.-W. Moon, C. Hwang, and K.-J. Kim, “Omnidirectional spin-wave array antenna,” *Physical Review Applied* **11**, 024027 (2019).
- ²⁶ “See supplemental information at [url].”
- ²⁷ D. R. Klein, D. MacNeill, J. L. Lado, D. Soriano, E. Navarro-Moratalla, K. Watanabe, T. Taniguchi, S. Manni, P. Canfield, J. Fernández-Rossier, *et al.*, “Probing magnetism in 2d van der waals crystalline insulators via electron tunneling,” *Science* **360**, 1218–1222 (2018).
- ²⁸ Y.-J. Chen, Kh. Zakeri, A. Ernst, H. J. Qin, Y. Meng, and J. Kirschner, “Group velocity engineering of confined ultrafast magnons,” *Physical Review Letters* **119**, 267201 (2017).
- ²⁹ H. J. Qin, S. Tsurkan, A. Ernst, and Kh. Zakeri, “Experimental realization of atomic-scale magnonic crystals,” *Physical Review Letters* **123**, 257202 (2019).
- ³⁰ L. Chen, J.-H. Chung, B. Gao, T. Chen, M. B. Stone, A. I. Kolesnikov, Q. Huang, and P. Dai, “Topological spin excitations in honeycomb ferromagnet CrI_3 ,” *Physical Review X* **8**, 041028 (2018).
- ³¹ S. M. Rezende, *Fundamentals of Magnonics*, Vol. 969 (Springer, 2020).
- ³² S. Zhang, R. Xu, N. Luo, and X. Zou, “Two-dimensional magnetic materials: structures, properties and external controls,” *Nanoscale* **13**, 1398–1424 (2021).
- ³³ D. Torelli, K. S. Thygesen, and T. Olsen, “High throughput computational screening for 2D ferromagnetic materials: the critical role of anisotropy and local correlations,” *2D Materials* **6**, 045018 (2019).
- ³⁴ D. Cortés-Ortuño and P. Landeros, “Influence of the dzyaloshinskii-moriya interaction on the spin-wave spectra of thin films,” *Journal of Physics: Condensed Matter* **25**, 156001 (2013).
- ³⁵ K. Wang, A. A. Puretzky, Z. Hu, B. R. Srijanto, X. Li, N. Gupta, H. Yu, M. Tian, M. Mahjouri-Samani, X. Gao, *et al.*, “Strain tolerance of two-dimensional crystal growth on curved surfaces,” *Science advances* **5**, eaav4028 (2019).
- ³⁶ Z. Peng, X. Chen, Y. Fan, D. J. Srolovitz, and D. Lei, “Strain engineering of 2d semiconductors and graphene: from strain fields to band-structure tuning and photonic applications,” *Light: Science & Applications* **9**, 1–25 (2020).
- ³⁷ A. Castellanos-Gomez, R. Roldán, E. Cappelluti, M. Buscema, F. Guinea, H. S. J. van-der Zant, and G. A. Steele, “Local strain engineering in atomically thin MoS_2 ,” *Nano letters* **13**, 5361–5366 (2013).
- ³⁸ Y. Sun and K. Liu, “Strain engineering in functional two-dimensional materials,” *Journal of Applied Physics* **125**, 082402 (2019).
- ³⁹ E. Khestanova, F. Guinea, L. Fumagalli, A. K. Geim, and I. V. Grigorieva, “Universal shape and pressure inside bubbles appearing in van der waals heterostructures,” *Nature Communications* **7**, 1–10 (2016).
- ⁴⁰ Z. Dai, L. Liu, and Z. Zhang, “Strain engineering of 2d materials: issues and opportunities at the interface,” *Advanced Materials* **31**, 1805417 (2019).
- ⁴¹ J. Quereda, P. San-Jose, V. Parente, L. Vaquero-Garzon, A. J. Molina-Mendoza, N. Agraït, G. Rubio-Bollinger, F. Guinea, R. Roldán, and A. Castellanos-Gomez, “Strong modulation of optical properties in black phosphorus through strain-engineered rippling,” *Nano letters* **16**, 2931–2937 (2016).
- ⁴² S. Yang, Y. Chen, and C. Jiang, “Strain engineering of two-dimensional materials: Methods, properties, and applications,” *InfoMat* **3**, 397–420 (2021).
- ⁴³ S. Deng, A. V. Sumant, and V. Berry, “Strain engineering in two-dimensional nanomaterials beyond graphene,” *Nano Today* **22**, 14–35 (2018).
- ⁴⁴ J. Jiang, T. Xu, J. Lu, L. Sun, and Z. Ni, “Defect engineering in 2D materials: precise manipulation and improved functionalities,” *Research* **2019** (2019).
- ⁴⁵ B. Schuler, D. Y. Qiu, S. Refaely-Abramson, C. Kastl, C. T. Chen, S. Barja, R. J. Koch, D. F. Ogletree, S. Aloni, A. M. Schwartzberg, *et al.*, “Large spin-orbit splitting of deep in-gap defect states of engineered sulfur vacancies in monolayer WS_2 ,” *Physical Review Letters* **123**, 076801 (2019).
- ⁴⁶ J. Mulkers, B. Van W., and M. V. Milošević, “Tunable snell’s law for spin waves in heterochiral magnetic films,” *Physical Review B* **97**, 104422 (2018).
- ⁴⁷ Z. Wang, B. Zhang, Y. Cao, and P. Yan, “Probing the dzyaloshinskii-moriya interaction via the propagation of spin waves in ferromagnetic thin films,” *Physical Review Applied* **10**, 054018 (2018).
- ⁴⁸ S. Macke and D. Goll, “Transmission and reflection of spin waves in the presence of néel walls,” *Journal of Physics: Conference Series*, **200**, 042015 (2010).
- ⁴⁹ X.-G. Wang, G.-H. Guo, G.-F. Zhang, Y.-Z. Nie, and Q.-L. Xia, “Spin-wave resonance reflection and spin-wave induced domain wall displacement,” *Journal of Applied Physics* **113**, 213904 (2013).
- ⁵⁰ F. t K de Vries, E. Portolés, G. Zheng, T. Taniguchi, K. Watanabe, T. Ihn, K. Ensslin, and P. Rickhaus, “Gate-defined josephson junctions in magic-angle twisted bilayer graphene,” *Nature Nanotechnology*, 1–4 (2021).
- ⁵¹ J. Mao, S. P. Milovanović, M. Anđelković, X. Lai, Y. Cao, K. Watanabe, T. Taniguchi, L. Covaci, F. M. Peeters, A. K. Geim, *et al.*, “Evidence of flat bands and correlated states in buckled graphene superlattices,” *Nature* **584**, 215–220 (2020).

- ⁵² X. Wang, Q. Weng, Y. Yang, Y. Bando, and D. Golberg, “Hybrid two-dimensional materials in rechargeable battery applications and their microscopic mechanisms,” *Chemical Society Reviews* **45**, 4042–4073 (2016).
- ⁵³ K. Zollner, P. E. F. Junior, and J. Fabian, “Proximity exchange effects in MoSe₂ and WSe₂ heterostructures with CrI₃: Twist angle, layer, and gate dependence,” *Physical Review B* **100**, 085128 (2019).
- ⁵⁴ Z. Y. Zhu, Y. C. Cheng, and U. Schwingenschlögl, “Giant spin-orbit-induced spin splitting in two-dimensional transition-metal dichalcogenide semiconductors,” *Physical Review B* **84**, 153402 (2011).
- ⁵⁵ J. A. Reyes-Retana and F. Cervantes-Sodi, “Spin-orbital effects in metal-dichalcogenide semiconducting monolayers,” *Scientific Reports* **6**, 1–10 (2016).